

Diverse Gaussian Noise Consistency Regularization for Robustness and Uncertainty Calibration

Theodoros Tsiligkaridis
MIT Lincoln Laboratory
ttsili@mit.edu

Athanasios Tsiligkaridis
Boston University
atsili@bu.edu

Abstract

Deep neural networks achieve high prediction accuracy when the train and test distributions coincide. In practice though, various types of corruptions occur which deviate from this setup and cause severe performance degradations. Few methods have been proposed to address generalization in the presence of unforeseen domain shifts. In particular, digital noise corruptions arise commonly in practice during the image acquisition stage and present a significant challenge for current robustness approaches. In this paper, we propose a diverse Gaussian noise consistency regularization method for improving robustness of image classifiers under a variety of noise corruptions while still maintaining high clean accuracy. We derive bounds to motivate and understand the behavior of our Gaussian noise consistency regularization using a local loss landscape analysis. We show that this simple approach improves robustness against various unforeseen noise corruptions by 4.2-18.4% over adversarial training and other strong diverse data augmentation baselines across several benchmarks. Furthermore, when combined with state-of-the-art diverse data augmentation techniques, experiments against state-of-the-art show our method further improves robustness accuracy by 3.7% and uncertainty calibration by 5.5% for all common corruptions on several image classification benchmarks.

1. Introduction

Deep neural networks are increasingly being used in computer vision and have achieved state-of-the-art performance on image classification [14, 21, 25]. However, when the test distribution differs from the train distribution, performance can suffer as a result, even for mild image corruptions and transformations [17]. In fact, models have unrealistic behavior when faced with out-of-distribution inputs that arise from synthetic corruptions [17], spatial transformations [8], and data collection setups [35, 40]. Although train/test distribution mismatch is common in practice, the problem has not

been thoroughly studied. Designing models that provide robustness to unforeseen deviations from the train distribution is highly desirable. Furthermore, calibrated uncertainty on data characterized by domain shifts is also desirable as users can know when models are likely to make errors, improving human-machine teaming.

The majority of the literature on robustness has focused on adversarial robustness against pixel-level ℓ_p norm-bounded perturbations [32, 47]. However, the ℓ_p norm-bounded perturbation model for corruptions does not account for common corruptions, such as rotation, translation, blur, and contrast changes, that are often encountered in practice. Semantic perturbations that alter image attributes while maintaining a natural look have been also shown to fool classifiers [22, 44]. Such domain shifts often correspond to large ℓ_p perturbations that circumvent defenses against imperceptible pixel-level perturbations. Sampling the entire space of possible image variations is not practical to protect models against test time failures, and knowledge of the test distribution is not warranted.

The natural approach to defending against a particular fixed distribution shift is to explicitly incorporate such data into the training process [23]. However, this paradigm has drawbacks including over-fitting to one type of corruption [10]; in [23], it was shown that ℓ_∞ robustness provides poor generalization to unforeseen attacks. The empirical study in [4] shows that several expensive methods improve robustness at the cost of lower clean accuracy or degraded uncertainty estimation and there are large trade-offs for various regularization methods. Data augmentation policies have been proposed to increase clean accuracy [6] based on reinforcement learning but are computationally expensive. Uncertainty calibration can be improved by simple ensembles [27] and pre-training [18]. However, it has been shown that calibration degrades significantly under domain shifts [34]. Recent work [16, 19] proposed diverse data augmentations to improve robustness and uncertainty calibration against common corruptions. However, robustness to noise corruptions remains a challenge.

Digital noise corruptions occur often in real world sce-

narios due to imaging sensors and/or other devices hardware imperfections, transmission losses, and environmental conditions [1, 12]. Image denoising methods have been proposed for certain noise distributions, e.g. Gaussian, impulse [1, 3] that rely on a-priori knowledge of noise statistics. Advances in this area have been made [2, 28] that do not place strong assumptions on or require much prior knowledge on noise distribution. However, these works focus on reconstruction quality, and not on robustness and uncertainty calibration under unforeseen noise corruptions. While denoising approaches can in principle be used in a learning pipeline by first cleaning noisy images and then using a standard classifier, this would (a) add an unnecessary layer of complexity to the task at hand since an additional model will have to be learned, (b) the noise that remains post-denoising might still fool classifiers at certain signal-to-noise ratios, and (c) it is unclear how robust this pipeline would be in the presence of unforeseen corruptions such as contrast, blur, etc. We propose a robust approach to recognition of corrupted images without any manual pre-processing/cleaning of input images that can potentially alter image content. Overall, the gap between accuracy/uncertainty in clean setting and noise domain shifts is still large; it remains an open question how to close this gap.

Present Work. We propose a training technique that enforces consistency between clean and noisy data samples at different scales to enhance robustness against unforeseen digital noise corruptions. Our approach can be characterized as a type of Gaussian data augmentation strategy coupled with consistency regularization. Viewed through the lens of local loss landscape regularity, our proposed consistency regularization method induces both a smoothing (curvature minimization) and flattening (gradient norm minimization) effect on the local loss landscape. Experimental results show that our method produces models that improve robustness in the presence of various practical unforeseen noise distribution shifts. Furthermore, the combination of our approach with more diverse data augmentations achieves state-of-the-art robustness and uncertainty calibration against all common corruptions.

Our contributions are summarized below:

1. We introduce a consistency loss based on the Kullback-Leibler (KL) divergence that embeds clean examples similarly to diverse Gaussian noise augmentations, and a corresponding training algorithm (DiGN).
2. We provide an analysis of our Gaussian noise consistency loss that uncovers an inducing effect of smoothing (minimizing curvature) and flattening (minimize gradient norm) of the local loss landscape. Furthermore, we derive probabilistic stability bounds that explicitly involve the local loss geometry characteristics. We additionally provide numerical evidence for this finding.

3. We experimentally show our approach outperforms several competitive baselines against various unforeseen noise corruptions on CIFAR-10-C, CIFAR-100-C, and Tiny-ImageNet-C datasets. Additionally, we show our approach can be effectively combined with diverse data augmentation methods to improve upon state-of-the-art robustness and uncertainty calibration against all common corruptions.

2. Background and Related Work

We assume labeled data of the form $(x, y) \sim \mathcal{D}$ drawn from distribution \mathcal{D} . The labels y correspond to C classes. Neural network function $f_\theta(\cdot)$ maps inputs into logits, and θ are the model parameters. The softmax layer is used to map logits into class probability scores given by $[p_\theta(x)]_c = e^{f_{\theta,c}(x)} / \sum_l e^{f_{\theta,l}(x)}$.

Standard Training. The standard criterion for training deep neural networks is empirical risk minimization (Standard):

$$\min_{\theta} \mathbb{E}_{(x,y) \sim \mathcal{D}} [\mathcal{L}(f_\theta(x), y)] \quad (1)$$

where the loss is chosen to be the cross-entropy function $\mathcal{L}(f_\theta(x), y) = -y^T \log p_\theta(x)$. While training using the criterion (1) yields high accuracy on clean test sets, network generalization performance to various data shifts may suffer.

Adversarial Training against ℓ_p Adversary. Adversarial training (AT) [32] is one of the most effective defenses against ℓ_p norm-bounded perturbations which minimizes the adversarial risk,

$$\min_{\theta} \mathbb{E}_{(x,y) \sim \mathcal{D}} \left[\max_{\|\delta\|_p \leq \epsilon} \mathcal{L}(f_\theta(x + \delta), y) \right] \quad (2)$$

During the training process, adversarial attacks are computed at inputs x that solve the inner maximization problem. The inner maximization may be solved iteratively using projected gradient descent (PGD) for norms $p \in \{2, \infty\}$, i.e., $\delta^{(k+1)} = \mathcal{P}_{B_p(\epsilon)}(\delta^{(k)} + \alpha \nabla_{\delta} \mathcal{L}(x + \delta^{(k)}, y))$ where $\mathcal{P}_{B_p(\epsilon)}(z) = \arg \min_{u \in B_p(\epsilon)} \|z - u\|_2^2$ is the orthogonal projection onto the constraint set. Frank-Wolfe optimization of the inner maximization is an alternative that offers increased transparency and geometric connections to loss landscape and attack distortion [41]. Another robust training approach that trades-off the natural and robust error using smoothing is TRADES [47]:

$$\min_{\theta} \mathbb{E}_{(x,y) \sim \mathcal{D}} \left[\mathcal{L}(f_\theta(x), y) + \lambda \max_{\|\delta\|_p \leq \epsilon} D(p_\theta(x) \parallel p_\theta(x + \delta)) \right] \quad (3)$$

where $D(\cdot \parallel \cdot)$ denotes the Kullback-Leibler divergence defined as $D(p \parallel q) = \sum_c [p]_c \log([p]_c / [q]_c)$ and the inner maximization is computed using PGD. Related works on defenses to adversarial perturbations include gradient

regularization [36], curvature regularization [33], and local linearity regularization [30].

These methods optimize robustness only inside the ϵ -ball of the training distribution which does not capture *perceptible* data shifts such as common image corruptions [17]. Training with arbitrarily large ϵ in the pixel-wise robustness formulations fails in practice as image quality degrades and clean accuracy suffers due to inherent tradeoff [42].

Random Self-Ensemble Training. In the context of adversarial robustness, a random self-ensemble (RSE) method has been proposed [31] based on noise injection at the input layer and each layer of neural networks and was demonstrated to provide good levels of robustness against white-box attacks. Considering noise at the input layer only, the RSE training criterion is:

$$\min_{\theta} \mathbb{E}_{(x,y) \sim \mathcal{D}} \left[\mathbb{E}_{\delta \sim \mathcal{N}(0, \sigma^2 I)} \mathcal{L}(f_{\theta}(x + \delta), y) \right] \quad (4)$$

and predictions are ensembled at inference time as $\hat{y}(x) = \arg \max_c \frac{1}{n} \sum_{i=1}^n [p_{\theta}(x + \delta_i)]_c$ where $\delta_i \sim \mathcal{N}(0, \sigma^2 I)$. This increases inference time due to the ensemble, is prone to overfitting at a fixed noise level σ , and cannot handle certain real-world corruptions well, such as contrast and fog.

Diverse Data Augmentation Training. A recent data augmentation technique, AugMix [19], was shown to achieve very strong performance against unforeseen corruptions by enforcing a consistency loss coupled with a diverse data augmentation scheme:

$$\min_{\theta} \mathbb{E}_{(x,y) \sim \mathcal{D}} \left[\mathcal{L}(f_{\theta}(x), y) + \lambda JS(p_{\theta}(x); p_{\theta}(x_{a,1}); p_{\theta}(x_{a,2})) \right] \quad (5)$$

where $JS(p_1; p_2; p_3) = \frac{1}{3}(D(p_1 \parallel p_{\text{mix}}) + D(p_2 \parallel p_{\text{mix}}) + D(p_3 \parallel p_{\text{mix}}))$ is the Jensen-Shannon divergence, $p_{\text{mix}} = \frac{1}{3}(p_1 + p_2 + p_3)$. The augmentations $x_{a,1}, x_{a,2}$ are transformations of x formed by mixing composition chains where each chain performs a random finite number of operations chosen from the set $\mathcal{A} = \{\text{rotate, posterize, shear-x, shear-y, translate-x, translate-y, solarize, equalize, autocontrast}\}$. Using diversity and randomness in choosing these operations and mixing weights at different levels of severity during training, this data augmentation method is empirically shown to significantly improve robustness against unforeseen corruptions in comparison to CutOut [7], MixUp [39, 46], CutMix [45], and AutoAugment [5] schemes. Fourier-based data augmentations have also been shown to be nearly as effective and can improve performance of AugMix further by including Fourier operations in the set \mathcal{A} [37].

A closely related data augmentation strategy, AugMax that combines diversity and hardness by first randomly sampling multiple augmentation operators and then learning an adversarial mixture of these operators, has been shown to be effective [43]. Another data augmentation technique shown

to improve performance against such image corruptions is DeepAugment [16], which distorts images by perturbing internal representations of image-to-image networks. These perturbations include zeroing, negating, convolving, transposing, applying activation functions, etc., and it generates semantically similar images for training.

While these diverse data augmentation frameworks offer good performance, they still have difficulty dealing with certain noise and blur-based corruptions which can be further improved upon.

Our Approach. We show that our Gaussian noise consistency regularization approach outperforms these methods under noise domain shifts, and when it is combined with diverse data augmentations, it achieves near state-of-the-art performance against unforeseen common corruptions.

3. Diverse Gaussian Noise Consistency Regularization

Our primary goal is to design a training method to improve generalization against a variety of noise corruptions while fitting in existing pipelines with minimal changes. We introduce a consistency loss that embeds representations of clean examples, x , and noisy examples, $x + \delta$, similarly. To increase resiliency against a variety of noise distributions, we diversify the perturbation statistics by choosing a random noise level σ uniformly in the range $[0, \sigma_{\text{max}}]$ and then generating the random perturbation $\delta \sim \mathcal{N}(0, \sigma^2 I)$.

Our proposed training criterion is:

$$\min_{\theta} \mathbb{E}_{(x,y) \sim \mathcal{D}} \left[\mathcal{L}(f_{\theta}(x), y) + \lambda \mathbb{E}_{\sigma \sim \mathcal{U}([0, \sigma_{\text{max}}])} \mathbb{E}_{\delta \sim \mathcal{N}(0, \sigma^2 I)} D(p_{\theta}(x) \parallel p_{\theta}(x + \delta)) \right] \quad (6)$$

where $p_{\theta}(\cdot)$ denotes the class probability scores and $D(\cdot \parallel \cdot)$ denotes the Kullback-Leibler divergence defined in Section 2. The classification loss $\mathcal{L}(f_{\theta}(x), y)$ in (6) maximizes accuracy on clean examples, while the consistency regularization terms force clean and noisy examples to have similar output distributions. Here, $\lambda \geq 0$ is a regularization parameter, \mathcal{U} denotes a uniform distribution, and $\mathcal{N}(0, \sigma^2 I)$ denotes the normal distribution with standard deviation σ .

We call our approach (6) Diverse Gaussian Noise consistency regularization, DiGN, and Algorithm 1 depicts our training procedure. A sample-based approximation is used to approximate the regularizer to maintain low computational complexity during training. In practice, a couple samples suffice to obtain strong robustness and uncertainty calibration. The concept is illustrated in Figure 1.

The motivation for placing distributions on scale parameters σ and associated noise perturbations δ to approximate (6) is to avoid memorization of fixed scale augmentations [10], which leads to poor generalization against various noise domain shifts. In contrast to RSE (4), which uses a fixed

Algorithm 1 DiGN pseudocode

Input: Training data $\{(x_i, y_i)\}$, Network f_θ , Training epochs T , Batch size $|B|$, learning rate schedule η_t , hyperparameters $(\lambda, \sigma_{\max}, n)$

Result: Trained network f_θ

for $t=0$ to $T-1$ **do**

for each batch $(x, y) \sim \mathcal{D}$ **do**

for sample $k \in \{1, \dots, n\}$ **do**

 Generate $\sigma^{(k)} \sim \mathcal{U}(0, \sigma_{\max})$ for each example

 Generate $\delta^{(k)} \sim \mathcal{N}(0, (\sigma^{(k)})^2 I)$ for each example

$$x_\delta^{(k)} = x + \delta^{(k)}$$

end for

$$R(x_i) = \frac{1}{n} \sum_{k=1}^n D(p_\theta(x_i) \parallel p_\theta(x_{i,\delta}^{(k)}))$$

$$\mathcal{L}_T(x_i, y_i) = \mathcal{L}(x_i, y_i) + \lambda R(x_i)$$

$$\theta = \theta - \eta_t \frac{1}{|B|} \sum_{i \in B} \nabla_\theta \mathcal{L}_T(x_i, y_i)$$

end for

end for

scale jointly with test-time ensembling at the same scale, we use a diverse set of Gaussian noise scales and do not rely on test-time ensembling. In contrast to AugMix (5), DiGN only makes use of Gaussian noise augmentations and leverages the Kullback-Leibler divergence instead of the Jensen-Shannon divergence as the consistency loss.

Interestingly, training with diverse Gaussian noise augmentations provides robustness not only against Gaussian noise, but also against a variety of weather, blur, noise and digital corruptions, as evidenced in our results. Our focus in this work is to design deep image classifiers that are robust to digital noise corruptions at different levels of severity, while also improving performance to all common corruptions when our method is combined with other complementary data augmentation methods, such as [19]. While this work improves upon the state-of-the-art in noise and all common corruptions, one limitation is that the hybrid combination of our theoretically-motivated approach and the heuristic diverse augmentations of AugMix does not provide a unified framework to encompass all corruptions and more complex distribution shifts.

3.1. Analysis of Gaussian Noise Consistency Regularization

In this section, we analyze the effect of Gaussian noise consistency regularization in the small-noise regime. Specifically, we obtain a relationship between loss curvature and Fisher information which is further used to derive a bound on the local loss deviation in a neighborhood of data examples. This bound aids in understanding the effect of Gaussian noise consistency regularization on the local loss landscape.

Using a second-order Taylor expansion on the KL diver-

gence, for small σ [26]:

$$D(p_\theta(x) \parallel p_\theta(x + \delta)) \approx \frac{1}{2} \delta^T G_\theta(x) \delta$$

where $G_\theta(x)$ is the Fisher information matrix (FIM) given by:

$$G_\theta(x) = \sum_k [p_\theta(x)]_k \nabla_x \log[p_\theta(x)]_k (\nabla_x \log[p_\theta(x)]_k)^T \quad (7)$$

Taking the expectation,

$$\mathbb{E}_{\delta \sim \mathcal{N}(0, \sigma^2 I)} D(p_\theta(x) \parallel p_\theta(x + \delta)) = \frac{\sigma^2}{2} \text{Tr}(G_\theta(x)) \quad (8)$$

where we used $\mathbb{E}_{\delta \sim \mathcal{N}(0, \sigma^2 I)} [\delta \delta^T] = \sigma^2 I$. Taking the outer expectation wrt. σ on approximation (8):

$$\begin{aligned} & \mathbb{E}_{\sigma \sim \mathcal{U}([0, \sigma_{\max}])} \mathbb{E}_{\delta \sim \mathcal{N}(0, \sigma^2 I)} D(p_\theta(x) \parallel p_\theta(x + \delta)) \\ & \approx \mathbb{E}_{\sigma \sim \mathcal{U}([0, \sigma_{\max}])} \left[\frac{\sigma^2}{2} \right] \text{Tr}(G_\theta(x)) = \frac{\sigma_{\max}^2}{6} \text{Tr}(G_\theta(x)) \quad (9) \end{aligned}$$

The FIM has a strong connection to curvature; in fact for the case of cross-entropy, the Hessian matrix of the loss function is identical to the FIM (7), as the next proposition shows.

Proposition 1. *The following relation holds $H(x) := \nabla_x^2 \mathcal{L}(f_\theta(x), y) = G_\theta(x)$.*

Thus, minimizing with the Gaussian noise regularizer (9) is equivalent to minimizing the curvature in all directions equally since $\text{Tr}(H(x)) = \sum_i \lambda_i(H(x))$, where λ_i denotes the sorted Hessian eigenvalues. This has the effect of inducing low curvature in the loss landscape of \mathcal{L} around x and encourages locally linear behavior.

What we show next is that there is another interesting effect that the KL smoothing regularizer induces. Substituting (7) into (9) and simplifying, we obtain:

$$\begin{aligned} & \mathbb{E}_{\sigma \sim \mathcal{U}([0, \sigma_{\max}])} \mathbb{E}_{\delta \sim \mathcal{N}(0, \sigma^2)} D(p_\theta(x) \parallel p_\theta(x + \delta)) \\ & \approx \frac{\sigma_{\max}^2}{6} \sum_k [p_\theta(x)]_k \|\nabla_x \log[p_\theta(x)]_k\|_2^2 \quad (10) \end{aligned}$$

This can be interpreted a regularization term that induces stability of predictions within a local neighborhood of x through weighted logit smoothing. This type of weighted logit smoothing leads to a bound on the local loss deviation.

Theorem 1. *The following bound holds on the loss function:*

$$\begin{aligned} |\mathcal{L}(x + \delta, y) - \mathcal{L}(x, y)| & \leq \|\delta\|_2 \|g(x)\|_2 \\ & \quad + \frac{1}{2} \lambda_{\max}(H(x)) \|\delta\|_2^2 + o(\|\delta\|_2^2) \quad (11) \end{aligned}$$

where $g(x) := \frac{\nabla_x \mathcal{L}(f_\theta(x), y)}{\sqrt{\sum_k y_k \|\nabla_x \log p(x)_k\|_2^2}}$

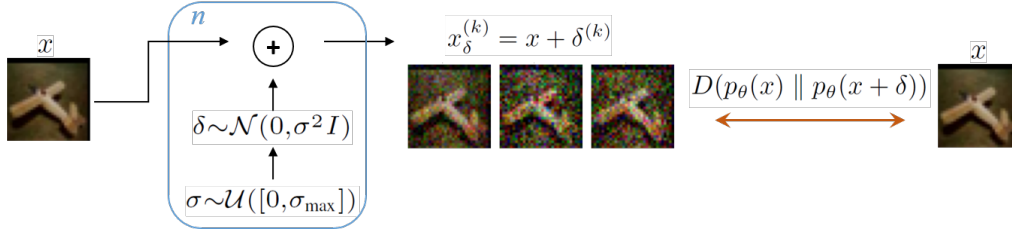


Figure 1. An illustration of our DiGN training methodology. During training, input images x are fed into n independent branches each associated with a new augmented sample. Each branch adds Gaussian noise δ to clean images controlled by a variety of scales σ sampled from a uniform distribution, and a consistency loss with respect to the clean images is formed.

A consequence of Theorem 1 is that for correct classifications where $y_k \approx p(x)_k$, minimizing the regularizer (10) has a twofold effect: (a) curvature is minimized, as the Hessian trace upper bounds the maximum Hessian eigenvalue of the loss $\mathcal{L}(x, y)$, $\lambda_{\max}(H(x)) \leq \text{Tr}(H(x))$, and (b) loss surface flatness is increased by minimizing the norm of the loss gradient, $\|\nabla_x \mathcal{L}(x, y)\|_2$. The joint effect of minimizing curvature and encouraging flatness in a neighborhood of x implies improved stability of the prediction as the loss changes are small with respect to small perturbations δ and as a result predictions are invariant to such perturbations.

Next we derive a probabilistic tail bound on the deviation from the true class probability under a Gaussian perturbation model that explicitly involves the gradient and Hessian of the loss function.

Theorem 2. *Let δ be a random vector drawn from the Gaussian distribution $\mathcal{N}(0, \sigma^2 I)$. For any $t > 0$, the stability bound holds:*

$$\mathbb{P} \left(\left| \ln \frac{[p(x)]_y}{[p(x + \delta)]_y} \right| > t \right) \leq C \exp \left(-\frac{t^2}{8d\sigma^2 \|g(x)\|_2^2} \right) + C \exp \left(-\frac{t}{2d\sigma^2 \lambda_{\max}(H(x))} \right)$$

where $C = 2^d$.

The probabilistic bound in Theorem 2 shows that the probability of the likelihood ratio $\left| \ln \frac{[p(x)]_y}{[p(x + \delta)]_y} \right|$ being large is vanishing exponentially fast at a rate proportional to $(d\sigma^2 \|g(x)\|_2^2)^{-1}$ and $(d\sigma^2 \lambda_{\max}(H(x)))^{-1}$. This stability result implies that the smaller the gradient norm and Hessian norm of the local loss are, the more stable the model is under random Gaussian perturbations. Since it is expected that models trained with DiGN exhibit loss surfaces with lower curvature and flatter neighborhoods, the true class likelihood score for noisy data $[p(x + \delta)]_y$ will remain close to that of clean data $[p(x)]_y$. The proofs of Theorems 1 and 2 are included in the supplementary material.

3.2. Empirical Validation

Figure 2 (top left) shows the validation loss difference $|\mathcal{L}(x + \delta, y) - \mathcal{L}(x, y)|$ to random perturbations δ of ℓ_2 radius ϵ for the CIFAR-10 validation set. These perturbations were generated by first sampling $u \sim \mathcal{N}(0, I)$, and setting $\delta = \epsilon \cdot u / \|u\|_2$. It is evident that our DiGN model maintains high validation accuracy (top right), reflected by the loss difference, against perturbations δ of increasing strength while the Standard model quickly degrades. The bottom left and right plots show the gradient norm and approximate curvature, which roughly represent the first order term given by $\epsilon \cdot \|\nabla \mathcal{L}(x, y)\|_2$, and second order term given by $\frac{1}{2} \epsilon^2 \cdot \text{Tr}(H^T H)$, of the bound (11). Here, we use a centered difference approximation of the curvature term $\text{Tr}(H^T H) = \mathbb{E}_{z \sim \mathcal{N}(0, I)} \|Hz\|_2^2 \approx \frac{1}{n} \sum_{i=1}^n \frac{1}{2\eta} \|\nabla \mathcal{L}(x + \eta z_i, y) - \nabla \mathcal{L}(x - \eta z_i, y)\|_2^2$ where $z_i \sim \mathcal{N}(0, I)$ and $\eta > 0$ is small. As expected from our theoretical analysis, our DiGN model has flatter gradients and lower curvatures than Standard training. This is a direct consequence of the loss geometry quantified in Theorem 1 that is induced by diverse Gaussian noise training (6).

4. Experimental Results

Datasets. The datasets used for our experimental results are (a) CIFAR-10, (b) CIFAR-100 [24], and (c) Tiny-ImageNet [29]. The CIFAR-10/100 datasets contain color images of size $32 \times 32 \times 3$ spanned across 50,000 train images and 10,000 test images, while Tiny-ImageNet contains color images of size $64 \times 64 \times 3$ spanned across 100,000 train images and 10,000 test images. Robustness against data shifts is measured by evaluating on CIFAR-10-C, CIFAR-100-C, and Tiny-ImageNet-C [17]. Each CIFAR corrupted dataset contains a total of $M = 18$ corruptions at $J = 5$ severity levels. The Tiny-ImageNet corrupted dataset contains $M = 14$ corruptions at $J = 5$ severity levels. The ‘gaussian noise’ corruption is excluded from our metric evaluations for fairness.

Computing infrastructure. All experiments were performed using 2 Volta V100 GPUs and 4 CPU cores. Methods were all implemented using the PyTorch deep learning

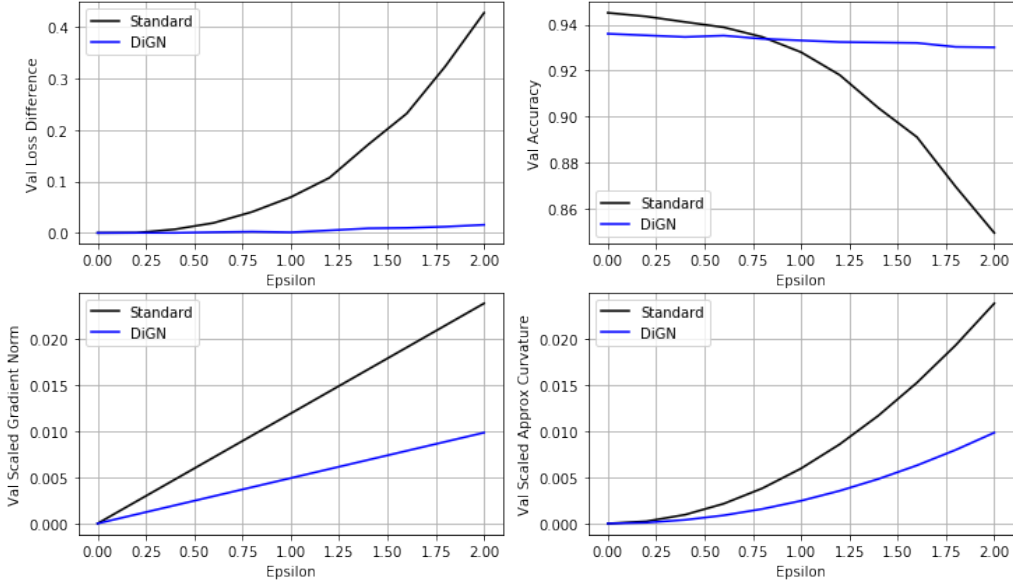


Figure 2. Model resilience against random perturbations δ of ℓ_2 radius ϵ for CIFAR-10 dataset on ResNet-18. Loss difference (top left), validation accuracy (top right), and local stability quantified by first (bottom left) and second order (bottom right) information are closely aligned. Our DiGN model maintains strong performance across a wide variety of perturbation strengths as opposed to Standard training which quickly degrades.

framework.

Baselines. The baseline methods considered include standard training (Standard), adversarial training (AT), tradeoff-inspired adversarial defense via surrogate-loss minimization (TRADES), random self-ensemble (RSE), diverse augmentation mixing chains (AugMix), deep augmentations (DeepAugment). The adversarial models based on AT and TRADES were trained against an ℓ_∞ adversary. The DeepAugment model was trained using the Noise2Net approach in [16] where randomly sampled image-to-image networks (composition of several randomized residual blocks using grouped convolutions) with random weights are used to generate deep image augmentations. We remark that AutoAugment is excluded from our comparisons because it was outperformed by a large margin by AugMix [19].

Training Details. The DiGN training method is demonstrated on deep residual network architecture ResNet-18 [15], densely connected convolutional architecture DenseNet-121 [20] and Wide-ResNet-18. The learning rate is started at 0.1 and decays every 50 epochs by a factor of 10. Pre-processing steps include standard random cropping, random horizontal flips, color jitter (0.25) and random rotation (2 degrees). Training was performed for 150 epochs using SGD with Nesterov momentum 0.9 and weight decay 0.0005. The model with the highest clean accuracy computed on the test set was selected as the best performer. For each performance metric, the mean and standard deviation over three independently trained model runs is reported.

The adversarial models based on AT and TRADES were trained using ℓ_∞ norm-bounded constraints using $\epsilon = 8/255$ and 7 PGD steps with step size $2.5\epsilon/7$ to allow sufficient exploration of the constraint set’s boundary. For RSE, a noise standard deviation $\sigma = 0.1$ for CIFAR-10/100 and $\sigma = 0.3$ for Tiny-ImageNet was chosen to achieve a high mCA experimentally with $n = 10$ samples used in test-time ensembling. For AugMix/AugMax, $\lambda = 12$ was chosen as in the original implementation. For DiGN, we use the following hyperparameters based on experimentation: $\sigma_{\max} = 0.2, \lambda = 0.2$ for CIFAR-10, $\sigma_{\max} = 0.2, \lambda = 0.3$ for CIFAR-100, and $\sigma_{\max} = 0.6, \lambda = 0.2$ for Tiny-ImageNet. For DeepAugment, we used Noise2Net hyperparameters $\epsilon = 0.1$, and 2 hidden planes for CIFAR-10/100, $\epsilon = 0.2$ and 2 hidden planes for Tiny-ImageNet.

Performance Metrics. Classification performance on the clean dataset is measured using test accuracy, i.e., $\frac{1}{n} \sum_{i=1}^n \mathbb{1}_{\{y_i = \hat{y}_i\}}$. Robustness against domain shifts is measured using accuracy on a corrupted validation set for different severity levels j . For a specific corruption type $m \in \{1, \dots, M\}$ and severity level $j \in \{1, \dots, J\}$, let $A_{m,j}$ denote the corresponding accuracy. The *mean corruption accuracy (mCA)* is defined as: $mCA = \frac{1}{MJ} \sum_{m=1}^M \sum_{j=1}^J A_{m,j}$. We denote the mCA score computed over only noise corruptions as $mCA-N$ (excluding Gaussian noise for fairness).

Classifier calibration scores measure how well the true empirical correct likelihood matches the predicted confidence. Calibration scores provide a signal for establish-

ing trust with human users with applications in safety in high-risk settings, out-of-distribution data detection and active learning. Uncertainty calibration performance is measured using the root-mean-square calibration error (*RMSE*), Expected Calibration Error (*ECE*) [13, 38], and Overconfidence Error (*OE*) [38]. In addition, we include a Sharpness (*SH*) metric inspired by [11]. To compute these metrics, we first partition the confidence interval $[0, 1]$ into n_B bins $\{B_i\}$ and denote the prediction confidence level as $c_j = \max_c [p_\theta(x_j)]_c$. The empirical accuracy and confidence of bin B_i is $\text{acc}(B_i) = \frac{1}{|B_i|} \sum_{j \in B_i} \mathbb{1}_{\{y_j = \hat{y}_j\}}$, and $\text{conf}(B_i) = \frac{1}{|B_i|} \sum_{j \in B_i} c_j$, respectively. *RMSE* measures the discrepancy between the empirical accuracy and the prediction confidence level as: $\text{RMSE} = \sqrt{\sum_{i=1}^{n_B} \frac{|B_i|}{n} (\text{acc}(B_i) - \text{conf}(B_i))^2}$. *ECE* is a very popular calibration metric that quantifies miscalibration as the absolute difference in expectation between confidence and accuracy as: $\text{ECE} = \sum_{i=1}^{n_B} \frac{|B_i|}{n} |\text{acc}(B_i) - \text{conf}(B_i)|$. *OE* penalizes predictions by the confidence when the confidence exceeds accuracy thus leading to high penalties for overconfident bins $\text{OE} = \sum_{i=1}^{n_B} \frac{|B_i|}{n} \text{conf}(B_i) \max\{\text{conf}(B_i) - \text{acc}(B_i), 0\}$. Sharpness measures precision or concentration of confidence intervals, which we define in our context as $\text{SH} = \left(\sqrt{\sum_{i=1}^{n_B} \frac{|B_i|}{n} \text{Var}(\{c_j\}_{j \in B_i})} \right)^{-1}$. Intuitively, the higher this SH metric is, the more concentrated predicted confidence levels are on the reliability plot across all bins. The notation $'-N'$ denotes computation only over noise corruptions (excluding Gaussian noise).

Robustness Results. Classification accuracy results computed on the clean and noise-corrupted CIFAR-10, CIFAR-100, and Tiny-ImageNet test sets are shown in Table 1 for various deep learning methods on the ResNet-18 architecture. For CIFAR-10, our method DiGN outperforms Standard baseline by 30.6% mCA-N absolute improvement, and outperforms previous state-of-the-art methods AugMix and DeepAugment by large margins of 5.9% and 4.2%, adversarial training baselines AT and TRADES by 11.6% and 13.1%, and RSE by 5.7%. Similarly, for CIFAR-100, DiGN outperforms Standard and AugMix training by 37.8% and 11.4% in mCA-N, respectively. For Tiny-ImageNet, DiGN outperforms Standard and AugMix training by 15% and 8.2% in mCA-N, respectively. Overall, DiGN consistently achieves the best accuracy against unforeseen digital noise corruptions across all datasets, yielding 4.2 – 18.4% boost, closing the gap between noise-corrupted and clean accuracy. Hyperparameters were experimentally chosen to achieve a high mCA-N score (see Supplementary Material for sensitivity analysis).

Next, we evaluate robustness against all common corruptions (noise, blur, weather, digital). Robustness results on digital noise and all common corruptions are shown

in Table 3 for CIFAR-10/100 datasets on DenseNet-121 and Wide-ResNet-18 architectures. The Wide-ResNet-18 architecture uses layer widths 320, 640, 1280, 2560 instead of 64, 128, 256, 512 used in ResNet-18. Our method DiGN continues to improve upon prior state-of-the-art AugMix by 9.3 – 14.0% in mCA-N. The hybrid combination DiGN + AugMix¹ outperforms AugMix by 2.1 – 3.7% in mCA and 7.0 – 13.2% in mCA-N. In addition, DiGN + AugMix outperforms AugMix by 1.5 – 5.5% in RMSE calibration error across all common corruptions.

The hybrid DiGN + AugMix consistently achieves the highest mCA and mCA-N scores improving upon previous state-of-the-art AugMix, implying that DiGN regularizes the model in a complementary way and improves generalization to a variety of digital noise corruptions that AugMix struggles with as shown in Table 1. We believe this is due to AugMix mostly attending to low-frequency variations, while DiGN adds a complementary benefit to robustness by providing resilience against high-frequency variations.

Uncertainty Calibration Results. Table 2 reports various calibration and sharpness metrics for the clean and noise corrupted test sets of CIFAR-10/100 on ResNet-18 architecture, which show that DiGN exhibits great calibration and sharpness scores, while simultaneously achieving the best mCA-N score. For CIFAR-10, DiGN outperforms Standard training by 24.8, 25.4, 22.9, 16.3%, and outperforms AugMix by 0.9, 0.9, 0.5, 17.1% in RMSE-N, ECE-N, OE-N and SH-N metrics, respectively. For CIFAR-100, DiGN outperforms Standard training by 25.1, 23.7, 16.3, 3.0%, and outperforms AugMix by 8.4, 7.9, 5.2, 1.8% in RMSE-N, ECE-N, OE-N and SH-N metrics, respectively. Overall, DiGN offers substantial improvements in RMSE, ECE and OE calibration errors and sharpness across all noise test sets and baseline methods while simultaneously achieving the state-of-the-art in mean corrupt accuracy. Furthermore, the hybrid combination DiGN + AugMix shown in Table 3 achieves the lowest RMSE on noise and all common corruptions for nearly all cases.

Ablation Study. We perform an ablation study to measure the benefit of consistency regularization (CR) in the DiGN objective (6) by comparing against training with diverse Gaussian noise augmentations directly in the cross-entropy loss (denoted as DiGNw.o.CR):

$$\min_{\theta} \mathbb{E}_{(x,y) \sim \mathcal{D}} \left[\mathbb{E}_{\sigma \sim \mathcal{U}([0, \sigma_{\max}])} \mathbb{E}_{\delta \sim \mathcal{N}(0, \sigma^2 I)} \mathcal{L}(f_{\theta}(x + \delta), y) \right] \quad (12)$$

Tables 1 and 2 show that DiGN with consistency regularization improves robustness, calibration and sharpness.

¹The training loss for this hybrid combination is formed by adding the Jensen-Shannon regularizer from (5) to the loss (6).

Table 1. Classification accuracy on clean CIFAR-10/CIFAR-100/Tiny-ImageNet datasets and Mean Corrupted Accuracy (mCA-N) on noise corruption subsets of CIFAR-10-C/CIFAR-100-C/Tiny-ImageNet-C datasets for ResNet-18 architecture.

Metric	Standard	AT	TRADES	RSE	DeepAugment	AugMix	AugMax	DiGNw.o.CR	DiGN
CIFAR-10									
Clean acc.	94.3±0.1	85.8±0.2	83.8±0.1	90.4±0.1	93.0±0.2	94.9±0.2	94.1±0.1	91.6±0.2	93.6±0.1
mCA-N	60.3±1.5	79.3±0.8	77.8±0.3	85.2±0.4	86.7±0.3	85.0±0.3	82.3±0.6	89.9±0.2	90.9±0.2
Gaussian Noise	48.1±1.6	80.5±0.8	79.0±0.2	87.4±0.3	87.1±0.4	80.2±0.4	75.3±1.1	90.1±0.2	91.1±0.1
Impulse Noise	57.1±2.0	75.6±0.7	74.1±0.4	80.2±0.4	82.8±0.2	84.6±0.2	82.6±0.8	89.1±0.1	89.4±0.2
Shot Noise	60.3±1.2	81.4±0.8	79.9±0.2	88.0±0.3	88.7±0.4	84.9±0.4	81.4±0.5	90.3±0.2	91.7±0.2
Speckle Noise	63.6±1.2	80.9±0.9	79.5±0.2	87.5±0.4	88.7±0.3	85.6±0.3	82.7±0.4	90.4±0.2	91.7±0.1
CIFAR-100									
Clean acc.	75.8±0.1	59.5±0.4	61.4±0.2	66.7±0.2	71.9±0.1	76.4±0.1	75.5±0.2	67.8±0.2	72.8±0.1
mCA-N	30.6±0.6	50.0±1.1	50.8±0.9	57.9±0.7	58.5±0.5	57.0±0.9	56.2±1.0	65.5±0.1	68.4±0.1
Gaussian Noise	21.4±0.6	51.1±0.8	53.4±0.6	61.5±0.9	57.2±0.6	47.8±1.1	45.5±1.0	65.3±0.1	68.6±0.0
Impulse Noise	28.6±0.5	37.8±1.6	43.7±1.4	49.0±0.7	55.1±0.3	60.3±0.5	61.7±1.2	64.0±0.1	66.0±0.2
Shot Noise	30.8±0.7	52.3±0.8	55.0±0.6	62.9±0.7	60.4±0.6	54.8±1.0	52.7±0.9	66.2±0.1	67.9±0.1
Speckle Noise	32.3±0.6	50.8±1.0	53.6±0.7	61.7±0.7	59.9±0.5	55.8±1.1	54.3±1.0	66.2±0.1	69.6±0.1
Tiny-ImageNet									
Clean acc.	59.1±0.4	45.5±0.2	46.3±0.4	34.3±7.8	54.9±0.2	60.4±0.1	56.7±4.3	51.3±0.3	56.0±0.2
mCA-N	24.5±0.5	28.3±0.1	27.7±0.5	23.5±5.7	26.0±1.2	31.3±1.3	30.1±1.2	37.3±0.2	39.5±0.7
Gaussian Noise	22.0±0.6	29.7±0.1	28.6±0.6	23.9±6.1	25.3±0.9	28.8±1.3	27.6±0.8	38.0±0.2	39.9±0.7
Impulse Noise	23.0±0.3	25.4±0.1	25.2±0.5	23.2±4.6	23.8±1.5	29.8±1.4	28.8±1.2	35.5±0.1	38.7±0.5
Shot Noise	25.9±0.7	31.1±0.1	30.1±0.5	23.9±6.7	28.2±0.9	32.8±1.1	31.3±1.1	39.0±0.3	40.2±0.8

Table 2. Uncertainty calibration (RMSE, ECE, OE) and sharpness (SH) metrics for clean and noise-corrupted CIFAR-10 and CIFAR-100 test sets on ResNet-18 architecture.

Metric	Standard	AT	TRADES	RSE	DeepAugment	AugMix	AugMax	DiGNw.o.CR	DiGN
CIFAR-10									
Clean RMSE	5.5±0.2	4.5±1.3	18.7±0.4	6.5±0.8	4.3±0.2	1.5±0.3	10.8±0.1	6.5±0.2	5.2±0.4
Clean ECE	3.3±0.0	2.9±0.8	16.7±0.4	4.4±0.5	2.5±0.1	1.0±0.2	8.7±0.1	4.2±0.1	3.1±0.1
Clean OE	2.9±0.0	0.4±0.3	0.0±0.0	3.8±0.5	2.2±0.1	0.0±0.0	0.0±0.0	3.8±0.1	2.8±0.1
Clean SH	108.3±0.5	61.6±1.1	56.2±0.3	79.9±1.6	85.5±0.6	68.4±1.4	57.8±0.1	85.3±0.7	94.1±0.9
Corrupt RMSE-N	30.4±1.7	2.2±1.0	16.7±0.5	9.8±0.5	5.8±0.2	6.5±0.3	3.7±0.2	7.1±0.2	5.6±0.2
Corrupt ECE-N	29.3±1.9	1.7±0.7	14.8±0.4	7.5±0.5	4.2±0.2	4.8±0.2	3.2±0.2	5.0±0.2	3.9±0.1
Corrupt OE-N	26.3±2.0	0.6±0.4	0.0±0.0	6.5±0.5	3.4±0.2	3.9±0.2	0.0±0.0	4.3±0.1	3.4±0.1
Corrupt SH-N	63.8±0.5	58.8±0.4	56.2±0.1	72.5±1.7	67.8±0.5	63.0±0.6	56.7±0.2	80.6±0.1	80.1±0.3
CIFAR-100									
Clean RMSE	8.5±0.1	5.2±2.3	4.0±1.2	13.1±0.4	11.2±0.7	2.8±0.3	17.2±0.5	11.9±0.1	6.5±0.3
Clean ECE	7.0±0.2	4.4±2.2	3.2±1.3	11.3±0.2	9.2±0.5	2.1±0.2	15.3±0.5	10.3±0.0	5.4±0.3
Clean OE	5.7±0.2	1.1±0.8	0.0±0.0	8.4±0.2	6.9±0.4	1.5±0.1	0.0±0.0	7.5±0.1	4.1±0.2
Clean SH	61.9±0.1	56.1±0.1	55.5±0.3	58.7±0.4	60.3±0.5	58.8±0.1	55.8±0.4	58.4±0.3	59.3±0.3
Corrupt RMSE-N	34.1±0.8	6.9±2.1	2.6±0.9	17.4±0.6	14.6±0.4	17.4±0.9	9.1±1.3	12.3±0.2	9.0±0.2
Corrupt ECE-N	31.5±0.8	6.2±1.9	2.2±0.7	15.6±0.7	13.2±0.3	15.7±0.9	8.3±1.2	10.8±0.2	7.8±0.2
Corrupt OE-N	22.1±0.8	2.6±1.9	0.3±0.4	11.3±0.5	9.2±0.2	11.0±0.8	0.0±0.0	7.7±0.2	5.8±0.1
Corrupt SH-N	55.4±0.1	55.9±0.1	55.7±0.0	57.1±0.0	56.7±0.1	56.6±0.1	56.0±0.0	57.8±0.2	58.4±0.1

5. Conclusion

A method for training robust deep learning classifiers is presented based on diverse Gaussian noise augmentation at different scales coupled with consistency regularization. It is analytically shown that our approach uncovers smoothing and flattening of the loss landscape. We empirically show that our method yields state-of-the-art robustness and uncertainty calibration under unforeseen noise domain shifts across different network architectures and datasets. In addition, our approach in combination with diverse data augmentations provides state-of-the-art robustness and uncertainty calibration under unforeseen common corruptions.

Table 3. Robustness and RMS calibration error for noise and all common corruptions on DenseNet-121 and Wide-ResNet-18.

Metric	Standard	AugMix	DiGN	DiGN + AugMix
CIFAR-10				
DenseNet-121				
Clean acc.	93.9±0.1	94.6±0.1	93.0±0.1	94.4±0.0
mCA-N	59.5±1.7	82.4±0.7	90.0±0.2	90.9±0.1
mCA	75.2±0.3	87.9±0.2	85.1±0.2	90.0±0.1
Clean RMSE	6.3±0.0	3.3±0.1	5.9±0.2	4.8±0.4
Corrupt RMSE-N	32.6±1.9	6.6±0.2	6.5±0.4	2.5±0.4
Corrupt RMSE	20.7±0.3	2.5±0.0	10.6±0.0	2.6±0.2
Wide-ResNet-18				
Clean acc.	94.5±0.2	95.5±0.3	94.3±0.0	95.9±0.1
mCA-N	62.0±1.6	85.7±0.4	91.8±0.2	92.7±0.1
mCA	78.9±0.6	90.0±0.2	87.7±0.3	92.1±0.1
Clean RMSE	4.91±0.0	1.9±0.2	4.3±0.5	2.0±0.2
Corrupt RMSE-N	29.0±1.2	8.7±0.5	5.2±0.2	3.4±0.3
Corrupt RMSE	16.1±0.5	5.1±0.5	8.1±0.5	3.6±0.5
CIFAR-100				
DenseNet-121				
Clean acc.	74.2±0.2	76.2±0.1	71.6±0.1	75.6±0.3
mCA-N	28.6±0.6	55.4±0.2	66.0±0.2	68.4±0.2
mCA	47.6±0.5	63.2±0.2	59.2±0.1	66.6±0.3
Clean RMSE	12.6±1.9	4.6±0.1	13.8±0.1	9.4±0.2
Corrupt RMSE-N	43.5±2.4	7.8±0.4	14.1±0.3	5.6±0.4
Corrupt RMSE	28.6±2.6	2.7±0.1	19.2±0.3	5.5±0.3
Wide-ResNet-18				
Clean acc.	75.3±0.6	77.0±0.5	75.3±0.4	77.6±0.2
mCA-N	39.2±2.5	58.8±0.5	70.5±0.4	72.0±0.2
mCA	55.1±0.6	65.9±0.5	64.7±0.5	69.6±0.3
Clean RMSE	5.2±0.1	3.6±0.5	6.1±0.3	3.3±0.6
Corrupt RMSE-N	21.6±2.2	20.8±0.3	4.1±0.0	8.9±0.3
Corrupt RMSE	11.7±0.6	10.1±0.3	4.7±0.2	4.6±0.2

Broader Impact

As modern deep neural networks are being deployed for safety-critical applications, such as healthcare, social media, autonomous driving, and biometrics, robustness and uncertainty quantification under a wide realistic variety of distribution shifts are important areas of study. These are critical for gaining public trust and avoiding denial of opportunity. Our work takes key steps in improving the performance and understanding of robust models for realistic noise distribution shifts, and our algorithm can be used as a simple plug-in to complementary data augmentation robustness methods to further enhance robustness and uncertainty calibration under various distribution shifts. While DiGN learns more robust feature representations under noise distribution shifts, users should consider potential limitations associated with data-driven ML predictions such as bias. Although this is not the primary focus of this work, while preliminary experiments show DiGN provides some level of ℓ_2 adversarial robustness, it remains an open question how to handle stronger adversarial attacks while simultaneously maintaining robustness across natural corruptions.

A. Appendix

A.1. Data Corruption Visualizations

An example image along with its corrupted versions is shown in Figure 3; although humans might be able to recognize this as a boat, a deep learning image classifier trained in a standard manner will fail against most of these corruptions.

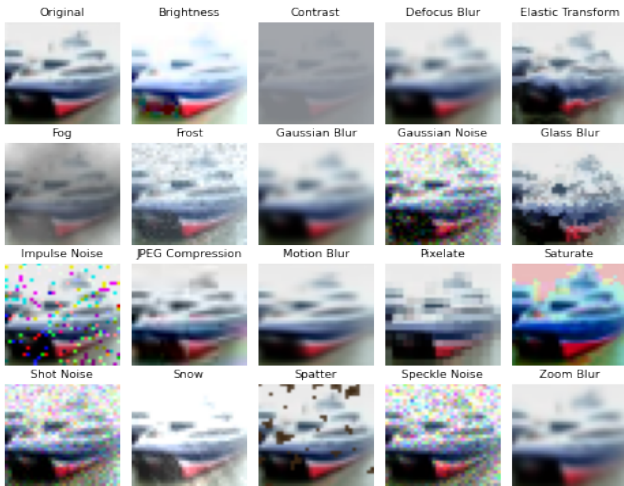


Figure 3. Example CIFAR-10 test image along with its corrupted versions. These corruptions are not available in the training process, and are only used for evaluation at inference time.

A.2. Proof of Proposition 1

Proof: The Hessian of the softmax cross-entropy function can be decomposed as (Appendix C in [30]):

$$H(x) = J^T(\text{diag}(p) - pp^T)J$$

where J denotes the Jacobian of the network function f_θ (logits) and p denotes the softmax probabilities. The Jacobian transposed is denoted as $J^T = [J_1^T, \dots, J_K^T]$ with $J_k := \nabla_x f_k(x)^T$. Starting from the FIM in (7), we have:

$$\begin{aligned} G_\theta(x) &= \sum_k p_k (\nabla_x \log p_k) (\nabla_x \log p_k)^T \\ &= \sum_k p_k (\nabla_x f_k - J^T p) (\nabla_x f_k - J^T p)^T \\ &= \sum_k p_k (\nabla_x f_k \nabla_x f_k^T - \nabla_x f_k p^T J \\ &\quad - J^T p \nabla_x f_k^T + J^T p p^T J) \\ &= \sum_k p_k \nabla_x f_k \nabla_x f_k^T - \left(\sum_k p_k \nabla_x f_k \right) p^T J \\ &\quad - J^T p \left(\sum_k p_k \nabla_x f_k \right)^T + J^T p p^T J \\ &= \sum_k p_k \nabla_x f_k \nabla_x f_k^T \\ &\quad - J^T p p^T J - J^T p p^T J + J^T p p^T J \\ &= \sum_k p_k J_k^T J_k - J^T p p^T J \\ &= J^T \text{diag}(p) J - J^T p p^T J \\ &= J^T (\text{diag}(p) - pp^T) J \\ &= H(x) \end{aligned}$$

This concludes the proof. \square

A.3. Proof of Theorem 1

Proof: Using the quadratic loss approximation near x , we have:

$$\mathcal{L}(x+\delta, y) = \mathcal{L}(x, y) + \delta^T \nabla_x \mathcal{L}(x, y) + \frac{1}{2} \delta^T H(x) \delta + o(\|\delta\|_2^2)$$

By using up to second order terms, an upper bound on the loss variation holds as:

$$\begin{aligned} &|\mathcal{L}(x + \delta, y) - \mathcal{L}(x, y)| \\ &\approx |\langle \nabla_x \mathcal{L}(x, y), \delta \rangle + \frac{1}{2} \delta^T H(x) \delta| \\ &\leq \|\delta\|_2 \cdot \|\nabla_x \mathcal{L}(x, y)\|_2 + \frac{1}{2} \delta^T H(x) \delta \quad (13) \end{aligned}$$

where we used the triangle inequality, and the Cauchy-Schwarz inequality to bound the linear term and the fact

that $H(x)$ is positive semidefinite. The gradient in the first term of (13) can be written as:

$$\begin{aligned} & \|\nabla_x \mathcal{L}(x, y)\|_2 \\ &= \sqrt{\left\| \sum_k -y_k \nabla_x \log p(x)_k \right\|_2^2} = \sqrt{\sum_k y_k \|\nabla_x \log p(x)_k\|_2^2} \\ &= \sqrt{\sum_k e_k \|\nabla_x \log p(x)_k\|_2^2 + \sum_k p(x)_k \|\nabla_x \log p(x)_k\|_2^2} \end{aligned}$$

where $e_k = y_k - p(x)_k$ is the prediction error. The quadratic form in (13) can be upper bounded using the eigenvalue bound:

$$\delta^T H(x) \delta \leq \lambda_{\max}(H(x)) \|\delta\|_2^2$$

Using the two preceding bounds into (13), the desired bound (11) is obtained. The proof is complete. \square

A.4. Proof of Theorem 2

For this proof, we first establish a tail bound on the ℓ_2 norm of random perturbations δ in the following lemma.

Lemma 1. *Consider δ drawn from the Gaussian distribution $\mathcal{N}(0, \sigma^2 I)$. Then, the following tail bound holds on the norm:*

$$\mathbb{P}(\|\delta\|_2 > u) \leq C \exp\left(-\frac{u^2}{2d\sigma^2}\right) \quad (14)$$

where $C = 2^d$.

Proof: Using Markov's inequality, we obtain for $s > 0$:

$$\begin{aligned} \mathbb{P}(\|\delta\|_2 > u) &\leq \mathbb{P}(\|\delta\|_1 > u) \\ &\leq e^{-su} \mathbb{E}[e^{s\|\delta\|_1}] \\ &= e^{-su} \mathbb{E}\left[\prod_{i=1}^d e^{s\sigma|z_i|}\right] \\ &= e^{-su} \prod_{i=1}^d \mathbb{E}[e^{s\sigma|z_i|}] \\ &= e^{-su} (\mathbb{E}[e^{s\sigma|z_1|}])^d \end{aligned} \quad (15)$$

where we used the decomposition $\|\delta\|_1 \equiv \sum_{i=1}^d \sigma|z_i|$ for standard normal variables z_i . The folded normal random variable $|z_1|$ has the moment generating function:

$$\begin{aligned} \mathbb{E}[e^{v|z_1|}] &= 2e^{\sigma^2 v^2/2} \Phi(\sigma v) \\ &= e^{\sigma^2 v^2/2} (1 + \operatorname{erf}\left(\frac{\sigma v}{\sqrt{2}}\right)) \end{aligned}$$

Using this result in (15), we obtain:

$$\begin{aligned} \mathbb{P}(\|\delta\|_2 > u) &\leq e^{-su} (\mathbb{E}[e^{s\sigma|z_1|}])^d \\ &\leq e^{-su} (e^{\sigma^2 s^2 u^2/2} (1 + \operatorname{erf}\left(\frac{\sigma s u}{\sqrt{2}}\right)))^d \\ &\leq 2^d e^{-su} e^{d\sigma^2 s^2 u^2/2} \end{aligned}$$

Optimizing the rate by choosing $s = u/(d\sigma^2)$, the bound simplifies to (14). This concludes the proof. \square

Now, we can proceed with the proof of Theorem 2.

Proof: We have for any $t > 0$:

$$\begin{aligned} \mathbb{P}\left(\left|\ln \frac{[p(x)]_y}{[p(x+\delta)]_y}\right| > t\right) &= \mathbb{P}(|\mathcal{L}(x, y) - \mathcal{L}(x + \delta, y)| > t) \\ &\stackrel{(a)}{\leq} \mathbb{P}(\|\delta\|_2 \|g\|_2 + \frac{1}{2} \lambda_{\max}(H) \|\delta\|_2^2 > t) \\ &\stackrel{(b)}{\leq} \mathbb{P}(\max\{\|\delta\|_2 \|g\|_2, \frac{1}{2} \lambda_{\max}(H) \|\delta\|_2^2\} > \frac{t}{2}) \\ &\stackrel{(c)}{\leq} \mathbb{P}(\{\|\delta\|_2 \|g\|_2 > \frac{t}{2}\} \cup \{\frac{1}{2} \lambda_{\max}(H) \|\delta\|_2^2 > \frac{t}{2}\}) \\ &\stackrel{(d)}{\leq} \mathbb{P}(\|\delta\|_2 > \frac{t}{2\|g\|_2}) + \mathbb{P}(\|\delta\|_2 > \sqrt{\frac{t}{\lambda_{\max}(H)}}) \end{aligned}$$

where for (a) we used Theorem 1, for (b) $A + B \leq 2 \max\{A, B\}$, for (c) $\{\max\{U, V\} > c\} \subseteq \{U > c\} \cup \{V > c\}$, for (d) we used the union bound. Using the tail bound from Lemma 1 twice concludes the proof. \square

A.5. Additional results Robustness and Uncertainty Calibration Performance on ResNet-18

Classification accuracy results on clean data and common corruptions are presented in Table 4 for CIFAR-10, CIFAR-100 and Tiny-ImageNet on ResNet-18. We observe that DiGN achieves high mCA scores improving upon Standard training by 8.6%, 11.0% and 3.0% for the CIFAR-10, CIFAR-100, and Tiny-ImageNet datasets respectively. This hybrid combination improves upon state-of-the-art by 0.6 – 3.0% mCA and 2.1 – 10.6% across datasets. Table 4. Robustness and RMS calibration error on all common corruptions on ResNet-18 architecture.

Metric	Standard	AugMix	AugMax	DiGN	DiGN + AugMix
CIFAR-10					
mCA	77.7±0.3	89.3±0.1	88.2±0.2	86.3±0.2	90.7±0.1
Clean RMSE	5.5±0.2	1.5±0.3	10.8±0.1	5.2±0.4	2.2±0.3
Corrupt RMSE	17.1±0.2	3.1±0.3	8.1±0.1	9.5±0.3	1.0±0.2
CIFAR-100					
mCA	51.1±0.1	64.8±0.3	64.7±0.4	62.1±0.1	67.8±0.1
Clean RMSE	8.5±0.1	2.8±0.3	17.2±0.5	6.5±0.3	2.8±0.1
Corrupt RMSE	20.1±0.3	9.8±0.6	13.3±0.7	10.1±0.4	2.7±0.2
Tiny-ImageNet					
mCA	25.5±0.2	36.0±0.6	33.4±3.1	28.5±1.0	36.6±0.2
Clean RMSE	10.3±0.1	4.6±0.6	19.1±3.4	9.7±1.1	6.4±1.5
Corrupt RMSE	25.1±0.2	15.3±6.5	5.6±2.7	19.8±1.6	4.7±2.6

Table 5 contains uncertainty calibration results on ResNet-18. DiGN offers significant improvements in RMSE calibration errors over Standard training; specifically, an average absolute improvement in RMSE calibration error of 24.8%, 25.1% and 13.4% on the noise subsets of CIFAR-10-C, CIFAR-100-C and Tiny-ImageNet-C test sets, respectively. Furthermore, DiGN outperforms AugMix by 0.9%, 8.4% and 8.1% absolute RMSE calibration error improvement for noise subsets CIFAR-10-C, CIFAR-100-C and Tiny-ImageNet-C, respectively.

Table 5. RMS calibration error on clean CIFAR-10/CIFAR-100/Tiny-ImageNet datasets and noise corruption subsets (excluding 'gaussian noise') of CIFAR-10-C/CIFAR-100-C/Tiny-ImageNet-C datasets for ResNet-18 architecture. DiGN achieves a significant reduction in corrupt RMSE-N over Standard and AugMix training.

Metric	Standard	AT	TRADES	RSE	DeepAugment	AugMix	AugMax	DiGNw.o.CR	DiGN
CIFAR-10									
Clean RMSE	5.5±0.2	4.5±1.3	18.7±0.4	6.3±1.0	4.3±0.3	1.5±0.3	10.8±0.1	6.5±0.2	5.2±0.4
Corrupt RMSE-N	30.4±1.7	2.2±1.0	16.7±0.5	9.7±0.6	7.7±0.1	6.5±0.3	3.7±0.2	7.2±0.2	5.6±0.2
CIFAR-100									
Clean RMSE	8.5±0.1	5.2±2.3	4.0±1.2	12.9±0.5	10.2±0.1	2.8±0.4	17.2±0.5	11.9±0.1	6.5±0.3
Corrupt RMSE-N	34.1±0.8	6.9±2.1	2.6±0.9	17.4±0.6	15.7±0.1	17.4±0.9	9.1±1.3	12.3±0.2	9.0±0.2
Tiny-ImageNet									
Clean RMSE	10.3±0.1	8.2±0.3	10.4±0.3	18.0±0.6	7.6±0.8	4.6±0.6	19.1±3.4	10.6±0.1	9.7±1.1
Corrupt RMSE-N	28.9±0.3	2.2±0.4	3.6±0.2	24.1±0.4	19.4±0.6	23.6±8.3	7.3±4.5	16.2±0.4	15.5±0.8

A.6. Hyperparameter Sensitivity

We study the effect of the training hyperparameters ($\lambda, \sigma_{\max}, n$) on the robustness performance of DiGN training using the ResNet-18 architecture for CIFAR-10 and CIFAR-100 datasets. Table 6 contains the clean accuracy, mean corrupted accuracy over noise (mCA-N) and all corruptions (mCA). It is evident that the robustness performance is not too sensitive to the choice of hyperparameters.

Table 6. Sensitivity analysis on hyperparameters of our DiGN training method. Test set accuracy for CIFAR-10/100 and CIFAR-10/100-C datasets on ResNet-18 architecture are shown.

$\lambda, \sigma_{\max}, n$	Clean accuracy	mCA-N	mCA
CIFAR-10			
0.5, 0.2, 3	92.8±0.2	90.6±0.1	85.8±0.1
0.4, 0.2, 3	93.2±0.1	90.5±0.3	85.8±0.4
0.3, 0.2, 3	93.0±0.1	90.7±0.1	86.1±0.3
0.2, 0.2, 3	93.6±0.1	91.0±0.1	86.3±0.2
0.4, 0.2, 1	92.9±0.1	90.6±0.2	85.9±0.1
0.3, 0.2, 1	93.4±0.1	90.5±0.3	85.9±0.5
0.2, 0.2, 1	93.3±0.2	90.2±0.4	85.9±0.1
0.1, 0.2, 1	93.6±0.1	89.8±0.2	85.1±0.3
0.05, 0.2, 1	93.5±0.1	89.1±0.2	84.6±0.3
0.02, 0.2, 1	93.3±0.1	87.5±0.2	83.4±0.4
0.02, 0.3, 1	92.9±0.2	87.2±0.4	82.5±0.6
CIFAR-100			
0.4, 0.2, 3	72.1±0.1	68.2±0.3	61.8±0.2
0.3, 0.2, 3	72.8±0.1	68.5±0.1	62.1±0.1
0.2, 0.2, 3	73.1±0.1	68.2±0.4	62.0±0.4
0.05, 0.2, 1	74.4±0.1	65.4±0.1	60.2±0.1
0.02, 0.2, 1	74.4±0.1	62.2±0.1	58.7±0.2
0.02, 0.3, 1	73.3±0.3	62.0±0.3	58.4±0.3
0.3, 0.2, 1	73.0±0.2	67.9±0.3	61.7±0.1
0.2, 0.2, 1	73.3±0.1	67.7±0.3	61.4±0.2
0.1, 0.2, 1	74.2±0.2	67.1±0.2	60.8±0.3

A.7. Sensitivity to Consistency Regularization Function

Here, we empirically study how sensitive DiGN is to the choice of consistency regularizer by substituting Jensen-Shannon (JS) regularization in place of Kullback-Leibler (KL) regularization. Table 7 presents results on CIFAR-10 and CIFAR-100 with a JS divergence regularizer and compares with KL divergence regularization (as described in the paper). Our results show that DiGN with KL consistency regularization outperforms JS consistency regularization.

A.8. Additional Results on Higher Resolution Data

We provide robustness and uncertainty calibration results on the ImageNette dataset [9] in Table 8, which comprises of 10 classes sampled from ImageNet. The image resolution is

Table 7. DiGN experimental results with KL and JS consistency regularization for CIFAR-10 and CIFAR-100 datasets on ResNet-18 and Wide-ResNet-18 architectures.

Metric	DiGN-KL	DiGN-JS	DiGN-KL	DiGN-JS
CIFAR-10				
	ResNet-18	ResNet-18	Wide-ResNet-18	Wide-ResNet-18
Clean acc.	93.6±0.1	92.9±0.3	94.3±0.0	93.9±0.1
mCA-N	90.9±0.2	89.3±0.2	91.8±0.2	90.9±0.2
Gaussian Noise	91.1±0.1	89.4±0.2	92.1±0.3	91.0±0.1
Impulse Noise	89.4±0.2	87.5±0.2	90.2±0.2	89.2±0.2
Shot Noise	91.7±0.2	90.3±0.3	92.6±0.2	91.7±0.2
Speckle Noise	91.7±0.1	90.2±0.2	92.8±0.3	91.8±0.2
Clean RMSE	5.2±0.4	5.4±0.1	4.3±0.5	4.8±0.1
Corrupt RMSE-N	5.6±0.2	7.5±0.2	5.2±0.2	6.4±0.3
CIFAR-100				
	ResNet-18	ResNet-18	Wide-ResNet-18	Wide-ResNet-18
Clean acc.	72.8±0.1	73.0±0.3	75.3±0.4	74.4±0.3
mCA-N	68.4±0.1	66.1±0.2	70.5±0.4	68.3±0.3
Gaussian Noise	68.6±0.0	65.9±0.3	71.2±0.2	68.7±0.2
Impulse Noise	66.0±0.2	63.1±0.1	67.1±0.7	65.0±0.6
Shot Noise	69.7±0.1	67.6±0.3	72.2±0.3	70.0±0.2
Speckle Noise	69.6±0.1	67.4±0.2	72.1±0.3	69.8±0.2
Clean RMSE	6.5±0.3	8.8±0.5	6.1±0.3	4.6±0.3
Corrupt RMSE-N	9.0±0.2	12.0±0.6	4.1±0.0	6.2±0.3

224×224 and we use a ResNet-50 architecture for these experiments. The hyperparameters used for this experiment are $(\lambda, \sigma_{\max}, n) = (0.2, 1.2, 3)$. For this dataset, the Gaussian perturbations δ during training were post-multiplied with a binary mask m thus only perturbing 20% of the image pixels to achieve high accuracy.

Table 8. DiGN experimental results for ImageNette on ResNet-50 architecture.

Metric	Standard	DiGN
Clean acc.	93.1±0.1	92.8±0.3
mCA-N	48.0±0.7	50.8±0.7
mCA	42.8±0.7	43.7±0.5
Clean RMSE	6.4±1.0	6.9±0.4
Corrupt RMSE-N	37.7±0.3	32.4±1.2
Corrupt RMSE	39.1±1.0	37.8±1.3

References

- [1] A. Awad. Denoising images corrupted with impulse, gaussian, or a mixture of impulse and gaussian noise. Engineering Science and Technology, an International Journal, 22(3), 2019. 2
- [2] Adria Font Cavalrons. Improved noise2noise denoising with limited data. In IEEE/CVF Conference on Computer Vision and Pattern Recognition Workshops (CVPRW), 2021. 2
- [3] Bo-Hao Chen, Jia-Li Yin, and Ying Li. Image noise removing using semi-supervised learning on big image data. In IEEE Third International Conference on Multimedia Big Data, 2017. 2
- [4] S. Chun, S. J. Oh, S. Yun, D. Han, J. Choe, and Y. Yoo. An empirical evaluation on robustness and uncertainty of regularization methods. In ICML Workshop on Uncertainty and Robustness in Deep Learning, 2019. 1
- [5] Ekin Dogus Cubuk, Barret Zoph, Dandelion Mane, Vijay Vasudevan, and Quoc V. Le. Autoaugment: learning augmentation policies from data. In CVPR, 2018. 3
- [6] E. D. Cubuk, B. Zoph, D. Mane, V. Vasudevan, and Q. V. Le. Autoaugment: Learning augmentation strategies from data. In CVPR, 2019. 1
- [7] T. DeVries and G. W. Taylor. Improved regularization of convolutional neural networks with cutout. In arXiv:1708.04552, 2017. 3
- [8] L. Engstrom, B. Tran, D. Tsipras, L. Schmidt, and A. Madry. Exploring the landscape of spatial robustness. In ICML, 2019. 1
- [9] Fast.ai. Imagenette, 2020. 11
- [10] R. Geirhos, C. R. M. Temme, J. Rauber, H. H. Schutt, M. Bethge, and F. A. Wichmann. Generalisation in humans and deep neural networks. In NeurIPS, 2018. 1, 3
- [11] T. Gneiting, F. Balabdaoui, and A. E. Raftery. Probabilistic forecasts, calibration and sharpness, 2007. 7
- [12] R. C. Gonzalez and R. E. Woods. Digital Image Processing. Pearson, 2018. 2
- [13] C. Guo, G. Pleiss, Y. Sun, and K. Q. Weinberger. On calibration of modern neural networks. In ICML, 2017. 7
- [14] K. He, X. Zhang, S. Ren, and J. Sun. Delving deep into rectifiers: Surpassing human-level performance on imagenet classification. In ICCV, 2015. 1
- [15] K. He, X. Zhang, S. Ren, and J. Sun. Deep residual learning for image recognition. In CVPR, 2016. 6
- [16] D. Hendrycks, S. Basart, N. Mu, et al. The many faces of robustness: A critical analysis of out-of-distribution generalization. In ICCV, 2021. 1, 3, 6
- [17] Dan Hendrycks and Thomas Dietterich. Benchmarking neural network robustness to common corruptions and perturbations. In ICLR, 2019. 1, 3, 5
- [18] Dan Hendrycks, Kimin Lee, and Mantas Mazeika. Using pre-training can improve model robustness and uncertainty. In ICML, 2019. 1
- [19] D. Hendrycks, N. Mu, E. D. Cubuk, B. Zoph, J. Gilmer, and B. Lakshminarayanan. Augmix: A simple data processing method to improve robustness and uncertainty. In ICLR, 2020. 1, 3, 4, 6
- [20] Gao Huang, Zhuang Liu, Laurens van der Maaten, and Kilian Q Weinberger. Densely connected convolutional networks. In CVPR, 2017. 6
- [21] Yanping Huang, Youlong Cheng, Ankur Bapna, Orhan Firat, Mia Xu Chen, Dehao Chen, Hyoungho Lee, Jiquan Ngiam, Quoc V. Le, Yonghui Wu, and Zhifeng Chen. Gpipe: Efficient training of giant neural networks using pipeline parallelism. In NeurIPS, 2019. 1
- [22] A. Joshi, A. Mukherjee, S. Sarkar, and C. Hegde. Semantic adversarial attacks: Parametric transformations that fool deep classifiers. In ICCV, 2019. 1
- [23] D. Kang, Y. Sun, D. Hendrycks, T. Brown, and J. Steinhardt. Testing robustness against unforeseen adversaries. In arXiv pre-print arxiv:1908.08016, 2019. 1
- [24] Alex Krizhevsky, Vinod Nair, and Geoffrey Hinton. Cifar-10 and cifar-100 datasets, 2009. 5
- [25] A. Krizhevsky, I. Sutskever, and G. E. Hinton. Imagenet classification with deep convolutional neural networks. In Advances in Neural Information Processing Systems, 2012. 1
- [26] S. Kullback. Information Theory and Statistics. Dover, 1997. 4
- [27] Balaji Lakshminarayanan, Alexander Pritzel, and Charles Blundell. Simple and scalable predictive uncertainty estimation using deep ensembles. In NeurIPS, 2017. 1
- [28] Jaakko Lehtinen, Jacob Munkberg, Jon Hasselgren, Samuli Laine, Tero Karras, Miika Aittala, and Timo Aila. Noise2noise: Learning image restoration without clean data. In ICML, 2018. 2
- [29] Fei-Fei Li, Andrej Karpathy, and Justin Johnson. Tiny imagenet dataset - cs231n course stanford, 2014. 5
- [30] C. Lin, J. Martens, S. Goyal, D. Krishnan, K. Dvijotham, A. Fawzi, S. De, R. Stanforth, and P. Kohli. Adversarial robustness through local linearization. In NeurIPS, 2019. 3, 9
- [31] X. Liu, M. Cheng, H. Zhang, and C.-J. Hsieh. Towards robust neural networks via random self-ensemble. In ECCV, 2018. 3
- [32] A. Madry, A. Makelov, L. Schmidt, D. Tsipras, and A. Vladu. Towards deep learning models resistant to adversarial attacks. In ICLR, 2018. 1, 2
- [33] M. Moosavi-Dezfooli, J. Uesato, A. Fawzi, and P. Frossard. Robustness via curvature regularization, and vice versa. In IEEE Conference on Computer Vision and Pattern Recognition, 2019. 3
- [34] Yaniv Ovadia, Emily Fertig, Jie Ren, Zachary Nado D Sculley, Sebastian Nowozin, Joshua V Dillon, Balaji Lakshminarayanan, and Jasper Snoek. Can you trust your model's uncertainty? evaluating predictive uncertainty under dataset shift. In NeurIPS, 2019. 1
- [35] B. Recht, R. Roelofs, L. Schmidt, and V. Shankar. Unbiased look at dataset bias. In ICML, 2019. 1
- [36] S. Ros and F. Doshi-Velez. Improving the adversarial robustness and interpretability of deep neural networks by regularizing their input gradients. In AAAI Conference on Artificial Intelligence, 2018. 3

- [37] R. Soklaski, M. Yee, and T. Tsiligkaridis. Fourier-based augmentations for improved robustness and uncertainty calibration. In NeurIPS Workshop on Distribution Shifts, 2021. [3](#)
- [38] Sunil Thulasidasan, Gopinath Chennupati, Jeff Bilmes, Tanmoy Bhattacharya, and Sarah Michalak. On mixup training: Improved calibration and predictive uncertainty for deep neural networks. In NeurIPS, 2019. [7](#)
- [39] Yuji Tokozume, Yoshitaka Ushiku, and Tatsuya Harada. Between-class learning for image classification. In CVPR, 2018. [3](#)
- [40] A. Torralba and A. A. Efros. Unbiased look at dataset bias. In CVPR, 2011. [1](#)
- [41] T. Tsiligkaridis and J. Roberts. Understanding and increasing efficiency of frank-wolfe adversarial training. In IEEE Conference on Computer Vision and Pattern Recognition (CVPR), 2022. [2](#)
- [42] Dimitris Tsipras, Shibani Santurkar, Logan Engstrom, Alexander Turner, and Aleksander Madry. Robustness may be at odds with accuracy. In ICLR, 2019. [3](#)
- [43] H. Wang, C. Xiao, J. Kossaifi, Z. Yu, A. Anandkumar, and Z. Wang. Augmax: Adversarial composition of random augmentations for robust training. In NeurIPS, 2021. [3](#)
- [44] K. Xiao, L. Engstrom, A. Ilyas, and A. Madry. Noise or signal: The role of image backgrounds in object recognition. In ICLR, 2021. [1](#)
- [45] Sangdoon Yun, Dongyoon Han, Seong Joon Oh, Sanghyuk Chun, Junsuk Choe, and Youngjoon Yoo. Cutmix: Regularization strategy to train strong classifiers with localizable features. In ICCV, 2019. [3](#)
- [46] Hongyi Zhang, Moustapha Cisse, Yann Dauphin, and David Lopez-Paz. mixup: Beyond empirical risk minimization. In ICLR, 2017. [3](#)
- [47] H. Zhang, Y. Yu, J. Jiao, E. P. Xing, L. El Ghaoui, and M. I. Jordan. Theoretically principled trade-off between robustness and accuracy. In ICML, 2019. [1](#), [2](#)